Fatigue behaviour of high-strength low-alloy steel sheets: influence of loading direction and microstructure on microcrack initiation and growth

María Cecilia Marinelli
Instituto de Física Rosario – CONICET, Universidad Nacional de Rosario, Bv. 27 de febrero 210 bis, 2000 Rosario, Argentina
marinelli@ifir-conicet.gov.ar, https://orcid.org/0000-0003-3032-9918

Felipe Díaz
Departamento de Ingeniería Electromecánica, Universidad Tecnológica Nacional-Facultad Regional Rafaela-CONICET, Acuña 49, Rafaela, Santa Fe, Argentina
felipe.diaz@frra.utn.edu.ar, https://orcid.org/0000-0003-4998-5536

Raúl Bolmaro
Instituto de Física Rosario – CONICET, Universidad Nacional de Rosario, Bv. 27 de Febrero 210 bis, 2000 Rosario, Argentina
bolmaro@ifir-conicet.gov.ar, https://orcid.org/0000-0002-8218-6958

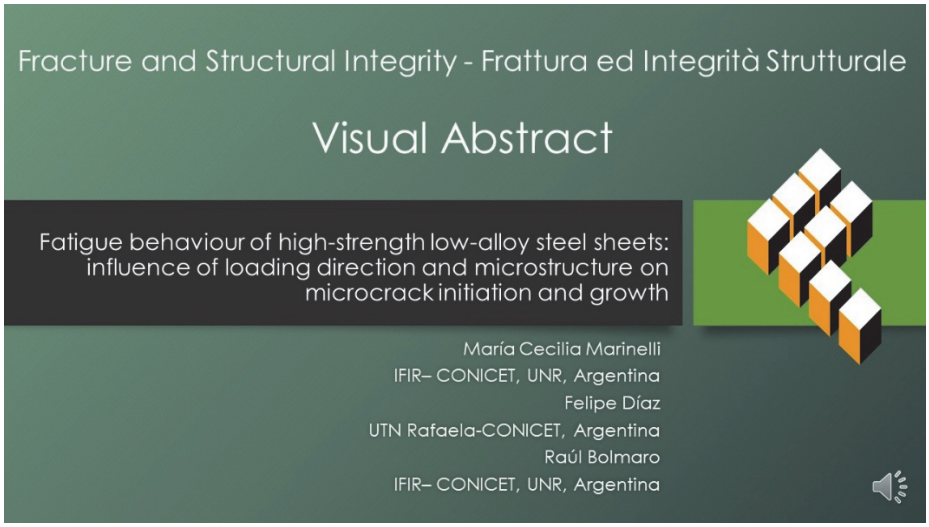

KEYWORDS. Multiaxial low cycle fatigue, Mechanical properties, HSLA steel sheet, Dislocation structures, Microcraks.

Citation: Marinelli, M. C., Diaz, F., Bolmaro, R., Fatigue behaviour of high-strength low-alloy steel sheets: influence of loading direction and microstructure on microcrack initiation and growth, Fracture and Structural Integrity, 74 (2025) 129-151.

Received: 30.07.2025
Accepted: 14.08.2025
Published: 18.08.2025
Issue: 10.2025

INTRODUCTION

One of the main challenges faced by the transportation and agricultural machinery industries is the weight of structural components, which leads to increased fuel consumption and greater environmental impact. Consequently, in recent years, there has been a growing interest in the sheet metal industry in producing thinner steel sheets that combine high strength with good formability [1]. These properties enhance payload capacity in transportation applications without compromising structural integrity while optimizing fuel efficiency.

Hot-rolled high-strength low-alloy (HSLA) steels are widely used in structural applications such as chassis components, front-side rails, engine mounts, wheels, rims, discs and suspension systems due to their advantageous combination of strength, weldability and formability. These steels typically have low carbon content and small additions of alloying elements like vanadium (V), niobium (Nb), titanium (Ti), manganese (Mn), and silicon (Si), which improve their mechanical properties compared to conventional carbon steels.

The high strength of HSLA steels, resulting from microstructural features such as grain refinement, precipitation hardening, and inclusion shape control, enables the use of thinner sheets, thereby reducing the overall weight of structural components. Simulation studies have shown that replacing conventional steels with HSLA-420 in trailer chassis structures can reduce weight by up to 20% without sacrificing strength [2]. However, despite their excellent static mechanical properties, HSLA steels remain susceptible to fatigue failure under cyclic loading. Fatigue, which accounts for nearly 90% of mechanical failures, can lead to catastrophic structural collapse at stress levels well below the ultimate tensile strength, making fatigue resistance a key design consideration.

In particular, the low-cycle fatigue (LCF) behaviour of HSLA steels is critically important for components subjected to limited cycles in the plastic regime. A deeper understanding of how microstructural parameters, such as crystallographic texture, grain size and phase distribution, influence the LCF response of HSLA steels is essential for improving lifetime predictions and ensuring the structural integrity of components subjected to cyclic plastic deformation. Despite its relevance, the literature contains limited research on the LCF performance of pearlite-reduced HSLA steels. Moreover, most experimental studies on sheet materials are typically conducted in a single orientation, usually either the rolling direction (RD) or the transverse direction (TD), without systematically evaluating anisotropic effects.

A recent study on S355MC and S460MC steels [3], conducted under fully reversed strain-controlled loading with specimens in the TD, offers useful reference data. The S460MC steel, microalloyed with niobium, exhibited higher yield and tensile strength but lower ductility than S355MC due to its finer grain structure. Both materials displayed a mixed cyclic response, transitioning from cyclic softening to hardening with increasing strain amplitude. This transition occurred earlier in S355MC, which led to reduced fatigue life at higher strain levels.

On the other hand, Fredriksson et al. [4] studied HSLA-500 under fully reversed strain-controlled loading conducted along the RD and reported cyclic softening and intermediate fatigue life compared to other advanced sheet steels such as DP600, DP400 and a deep-drawing quality (DDQ) steel. Similarly, Eifler et al. [5] investigated strain-controlled fatigue in plain carbon steels and demonstrated that the evolution of cyclic hardening or softening is closely linked to dislocation structures, particularly the formation of dislocation bands in ferrite grains, under varying plastic strain amplitudes. However, these studies did not consider directional effects within the sheet.

In contrast, Roven et al. [6] examined hot-rolled steels fatigued in the TD and provided valuable insight into the formation of substructures such as persistent slip bands, subgrains, and microbands, which are closely associated with fatigue crack nucleation. Milan et al [7] studied the monotonic and LCF behaviour under strain-controlled conditions in HSLA microalloyed with titanium in the RD and TD. They reported that specimens tensile tested in the TD exhibited higher yield and ultimate strengths, as well as greater ductility, compared to those tested in the RD. Regarding fatigue behaviour, meaningful results were obtained only for the TD condition, as the RD specimens experienced severe buckling during cyclic loading. In the TD direction, the material exhibited cyclic softening up to a total strain amplitude of 0.25%, followed by a characteristic softening-hardening sequence at higher strain amplitudes. The fatigue life of TD specimens was found to follow the Coffin-Manson strain-life relationship.

More recently, Paul et al. [8] analysed the LCF response of a hot-rolled low-carbon steel in the RD under various strain amplitudes. They found that cyclic softening was driven by substructural evolution, including the formation of dislocation cells at high strains, with fatigue cracks initiating at ferrite grains. Moreover, the fatigue life followed the empirical Coffin-Manson relation.

Despite the available knowledge, there is still a need to understand how sheet anisotropy affects the fatigue response and life of HSLA steels. Taking into account this need, the present work proposes a comparative study of low-cycle fatigue behaviour in HSLA-420 steel sheets, tested along the three principal directions: RD, TD, and 45° to rolling direction

(DD). The objective is to evaluate the directional effects on fatigue behaviour and life and to relate these findings to the crystallographic texture, dislocation substructure and, crack initiation and growth mechanisms.

MATERIAL AND EXPERIMENTAL PROCEDURE

Material

The material selected for the present study is a commercially available ferritic-pearlitic steel, designated HSLA-420 [1], provided as a hot-rolled sheet of 4.5 mm thickness. Its chemical composition is detailed in Tab. 1.

C	Si	Mn	P	S	Al	Ti	Nb
0.0780	0.1200	1.1900	0.0130	0.0046	0.0450	0.0240	0.0380

Table 1: Chemical composition of the HSLA-420 (in wt.%).

Specimen preparation and mechanical tests conditions

Microstructural characterization was conducted using optical microscopy (OM), scanning electron microscopy (SEM) and X-ray diffraction (XRD). Samples were prepared by standard mechanical polishing finished with 1 µm diamond paste and then etched with 2% Nital. Crystallographic texture analysis was performed using a Philips X'Pert Pro MPD diffractometer equipped with a Cu Kα radiation source. To calculate dislocation density, diffractograms were acquired using a scan step size of 0.02° and scan rate of 0.01°/s. Data were analysed by a Rietveld model as implemented in Maud software. Peak broadening was calculated by the Langford model [9], and domain sizes and dislocation densities by W-S equations [10].

Microhardness tests were carried out with a SHIMADZU MHV-2 microhardness tester using a load of 2.942N, HV 0.3. A total of 10 measurements were taken for the average hardness value.

Tensile tests were performed using an INSTRON 3382 universal testing machine. Specimens were extracted along three principal orientations of the sheet: the rolling direction (RD), transverse direction (TD, 90° to RD in the plane), and diagonal direction (DD, 45° to RD in the plane). For each orientation, three tensile specimens were prepared by the ASTM E8M standard, featuring a width of 6 mm and a gauge length of 32 mm (Fig. 1a). The tensile tests were performed at a constant crosshead speed of 0.5 mm/min until specimen fracture occurred. Each test was repeated at least three times to ensure reproducibility.

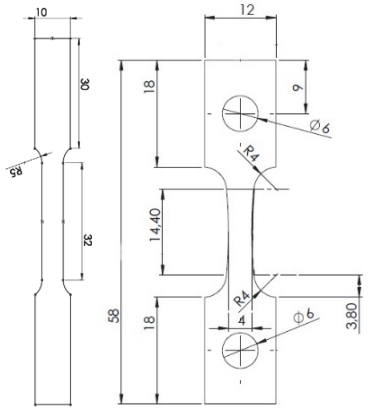

Figure 1: Details of the (a) tensile and (b) LCF test specimens (units in mm).

Low-cycle fatigue (LCF) tests were performed under fully reversed triangular wave loading (R = –1) at room temperature using an INSTRON 1362 electromechanical testing machine, under plastic strain control. The tests were conducted with plastic strain ranges of $\Delta\varepsilon_p$ = 0.1%, 0.2% and 0.3% at a total strain rate of $\dot{\varepsilon} = 2 \times 10^{-3}$ s^{-1}. Flat fatigue specimens were manufactured by electro erosion with a test length of 12.5 mm and a cross-section of 12 mm^2 (Fig. 1b) to compare the fatigue behaviour in the three characteristic directions of the sheet: RD, TD and DD. Each test was repeated at least

twice. The specimens were first ground and polished with sequentially finer grits up to 1μm diamond paste. After testing, the specimens were etched with 2% Nital solution for 10 seconds to reveal the microstructure. Additionally, the fatigue tests were extended to include intermediate plastic deformation ranges, i.e., $\Delta\varepsilon_p$ = 0.15% and 0.25%, to establish the traditional Coffin-Manson (C-M) relationship, as given in Eqn. (1). The number of cycles to failure (Nf) was defined as the number of cycles corresponding to a 30% reduction in the saturated tensile peak stress observed a few cycles before the final fracture. The fatigue ductility coefficient and exponent, B and c, respectively, were obtained from a linear regression on double-logarithmic plots of plastic strain amplitude ($\Delta\varepsilon_p/2$) versus the number of reversals to failure (2Nf). Linear regression was used as implemented in OriginPro 8.5 software.

$$\frac{\Delta\varepsilon_p}{2} = B(2Nf)^c \tag{1}$$

Transmission electron microscopy

Fatigue behaviour was correlated with the dislocation structure using a JEOL TEM operated at 200 kV in bright-field (BF) mode. Observations were performed near the zone axis to optimize diffraction contrast and enhance the visibility of dislocation arrangements and subgrain boundaries. Since the specimens were ferromagnetic, frequent microscope recalibration was required to maintain image stability and resolution. Thin foils were prepared from fatigued specimens cut longitudinally, i.e., along the tensile axis. The surface layer close to the specimen edge was mechanically ground with SiC abrasive papers of 400–600 grit until reaching a thickness below 100 μm. Discs of 3 mm in diameter were then punched from these regions and further thinned to electron transparency (<100 nm) using a twin-jet polishing unit (Struers TenuPol-5) with a 10% perchloric acid and 90% ethanol solution at −15 °C and 20.5 V.

RESULTS AND DISCUSSION

Material characterization

The microstructure of the HSLA-420 steel analysed in this study is presented in Fig. 2a. It predominantly consists of equiaxed ferrite grains with an average grain size of 6 ± 1 μm, accompanied by pearlite in two distinct morphologies: individual grains and regions distributed around the ferrite grain boundaries as indicated by the arrows in Fig. 2a. The volume fractions of ferrite and pearlite are approximately 80% and 20%, respectively, and the steel exhibits an average hardness of 165 ± 10 HV.

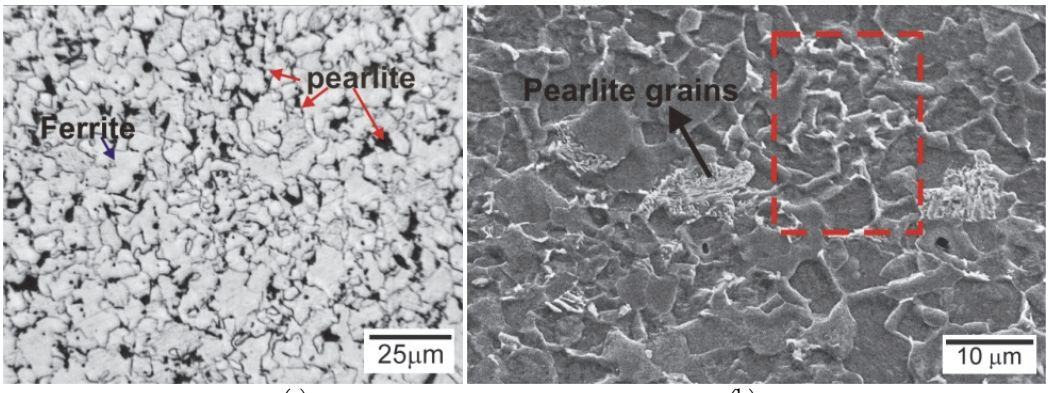

(a) (b)

Figure 2: HSLA-420. (a) Optical micrograph showing a ferrite-pearlite structure. The bright areas correspond to ferrite and the dark regions to pearlite; (b) SEM image showing a ferrite-pearlite microstructure. Pearlite appears brighter due to the presence of cementite, while ferrite appears as the darker phase.

While the ferrite and cementite layers within the pearlite are closely spaced and not resolved under optical microscopy, SEM (Fig. 2b) reveals distinct pearlite colonies characterized by cementite lamellae, which constitute the second phase. The lamellae thickness varies between the pearlite grains and some regions show non-uniform distributions of pearlite as enclosed in Fig. 2b. Further insights into the microstructure are provided in Fig. 3, which highlights the dislocation structures within the ferrite grains. A heterogeneous distribution of dislocations is observed in Fig. 3a, including features

such as dislocation tangles, wall-like dislocation structures, and interactions between dislocations and precipitates (highlighted in Fig. 3a). These characteristics are typical of ferritic-pearlitic steel sheets, where rolling induces dislocations that accumulate producing strain hardening [6,11]. Additionally, Fig. 3b shows randomly distributed cementite precipitates, while Fig. 3c provides a detailed view of pearlite as a lamellar structure composed of alternating ferrite and cementite layers. The average interlamellar spacing within the pearlite is 0.3 μm.

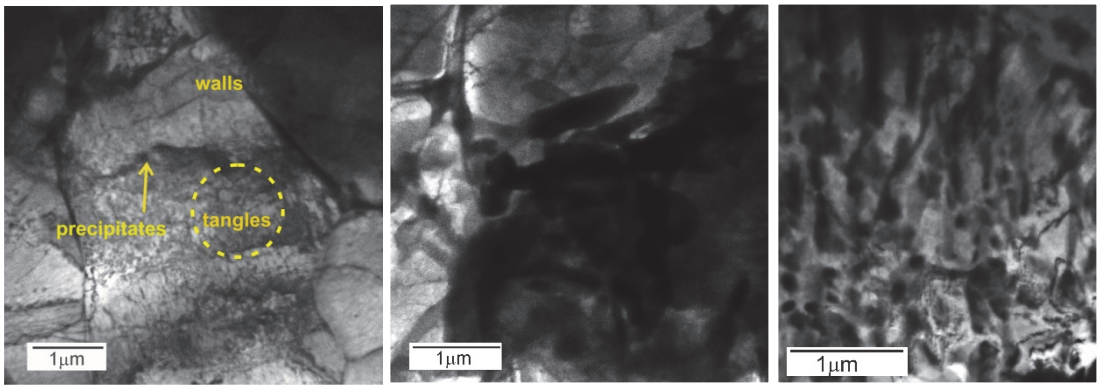

Figure 3: TEM BF micrograph showing dislocation structure in the as-received condition: (a) dislocation tangles, wall-like dislocation and dislocation-precipitate interactions in ferrite; (b) non-uniform distribution of cementite; (c) uniform distribution of cementite.

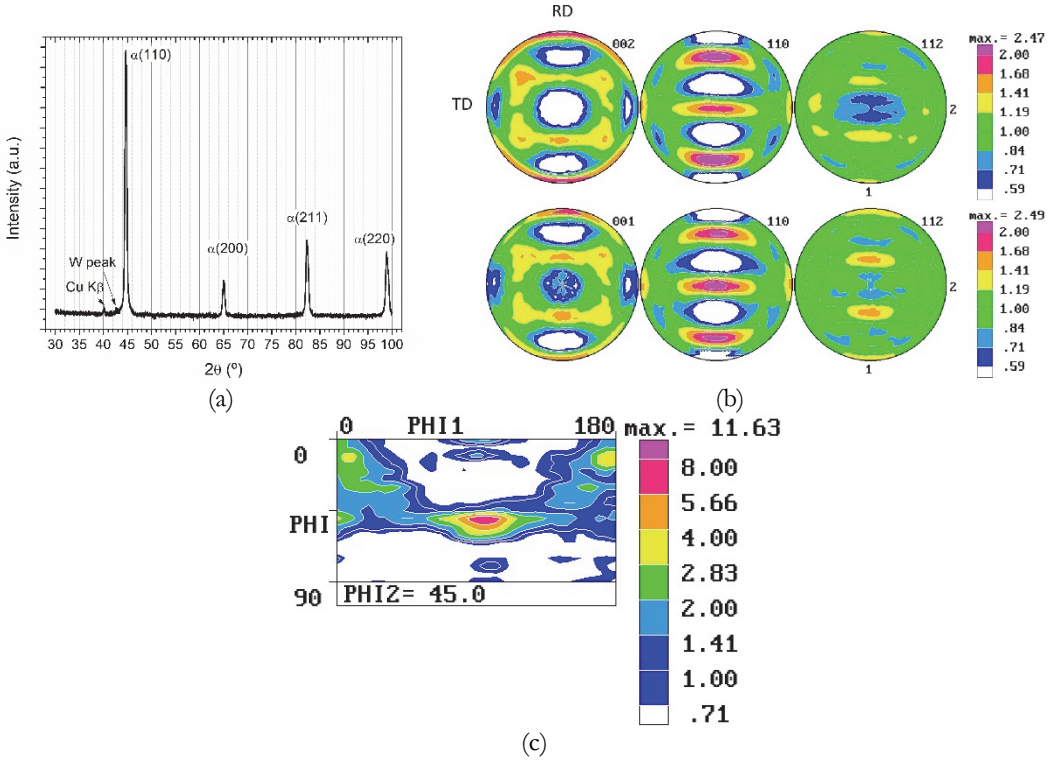

Figure 4: Texture analysis of HSLA-420: (a) X-ray Diffractogram; (b) Normalized experimental and recalculated pole figures; (c) Φ_2 = 45° ODF section.

The crystallographic texture of the HSLA-420 steel was analysed using XRD. The diffractogram presented in Fig. 4a indicates that, despite the steel containing approximately 20% pearlite, the diffraction peaks corresponding to cementite are scarcely visible. The nanometric spacing of cementite lamellae within the pearlite colonies induce an extreme peak broadening, resulting in low cementite peak intensities that are indistinguishable from background noise. Furthermore, the diffraction pattern is dominated by reflections from the ferrite phase, with the overall crystallographic texture governed by the body-centred cubic (BCC) ferrite matrix.

The global texture was determined using the Schulz reflection method, followed by correction and recalculation of the Orientation Distribution Function (ODF) from the measured pole figures. Fig. 4b displays both experimental and recalculated pole figures, revealing a moderately developed texture with a predominant alignment of crystallographic planes along the RD. The texture intensity is relatively low, with maxima around a multiple of random distribution (m.r.d.) value of approximately 2, indicating that the material exhibits only a slight preferential grain orientation.
A more in-depth analysis of the texture is provided by the ODF section at Phi2 = 45°, shown in Fig. 4c, which reveals a dominant α fibre (Phi1 = 0 with 0º>Phi>55º) and a partially developed γ fibre (Phi = 55º, 0º>Phi1>180º). Both features are characteristic of rolled BCC materials. The presence of the α fibre indicates a preferred alignment of grains with the <110> direction parallel to the rolling direction (RD), which is commonly associated with improved mechanical properties such as yield strength and ductility along this axis. The partially developed γ fibre suggests some retention of strain-induced orientations perpendicular to the normal direction (ND) (<111>//ND) together with recrystallization texture, product of intermediate heat treatments between deformation steps, which may affect anisotropic behaviour during subsequent mechanical loading. These texture characteristics provide important insights into the microstructural evolution during processing and their potential impact on the anisotropic mechanical response of the HSLA-420 steel. These components favour mechanical formability, making rolled products particularly suited for mechanical structures fabrication.

Tensile tests

Fig. 5 displays the Stress-Strain curves of the HSLA-420 steel in the RD, TD, and DD directions for a set of six samples. From these curves, key mechanical properties were extracted, including 0.2% offset yield strength ($\sigma_{y0.2}$), tensile strength (σ_{max}), uniform (ε_u) and total (ε_{total}) elongations. The mean values and associated standard deviations, indicative of the variability in the measurements, are summarized in Tab. 2.

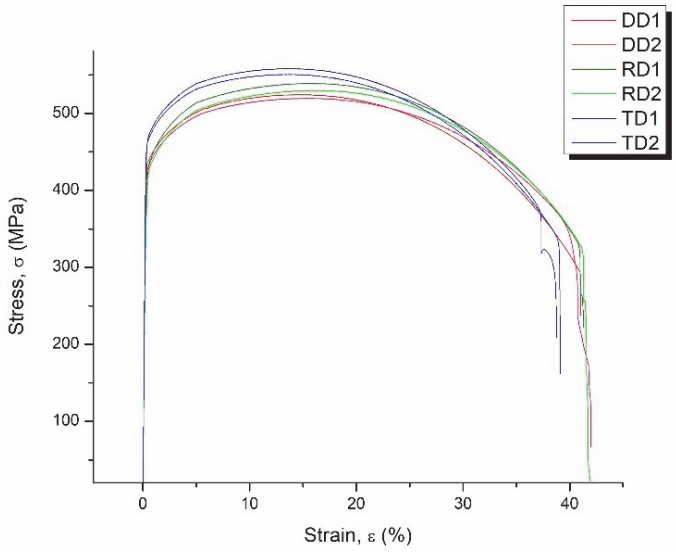

Figure 5: Tensile test curve of RD, TD and DD samples.

Sample	$\sigma_{y0.2}$ (MPa)	σ_{max} (MPa)	ε_u (%)	ε_{total} (%)	E (GPa)	K_f (MJ/m^3)
RD	420±5	530±5	16±0.5	40±1	160	200
DD	430±5	520±5	16±0.5	40±1	170	195
TD	465±5	560±5	14±0.5	38±1	180	195

Table 2: Data obtained from tensile test.

Additionally, the Young's modulus (E) was computed by fitting the linear region of the stress-strain curve, using a 20% segment of the linear portion and applying the least-squares regression method according to ASTM E8. The modulus of toughness (K_f) was evaluated by integrating the area under the entire stress-strain curve up to fracture. The data in Tab. 2 illustrates a favourable balance between strength and ductility in the HSLA-420 steel, demonstrating superior mechanical performance to other ferritic-pearlitic steels of comparable composition [12].

Notably, the tensile properties show minimal directional dependence, in accordance with the low severity of the texture. Specifically, the ratio of yield stress in the RD to the TD ($\sigma_{yRD}/\sigma_{yTD}$) is approximately 0.9, while the ratios for $\sigma_{yRD}/\sigma_{yDD}$ and $\sigma_{yDD}/\sigma_{yTD}$ are 0.97 and 0.92, respectively. This behaviour is consistent with the Hall-Petch relationship, which predicts an increase in the yield stress σ_y with decreasing average ferrite grain size d given in Eqn. 2 [12].

$$\sigma_y = \sigma_o + k.\ d^{-1/2} \quad (2)$$

In this expression, σ_o is the lattice resistance to dislocation movement and k is the grain boundary locking term measuring the hardening contribution by the grain boundaries. Using the average d values measured in the different directions (6 μm, 5 μm and 5.8 μm for RD, TD and DD, respectively) and the σ_y values from Tab. 2, the values obtained for σ_o and k were 51.5 MPa and 36.5 N.mm$^{-3/2}$, respectively. Fig. 6 shows the quasi-linear relationship between σ_y and $d^{-1/2}$.

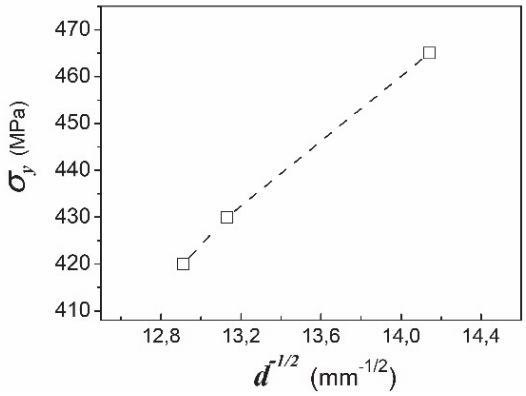

Figure 6: Hall-Petch relationship based on grain size (d) measurements in the RD, DD, and TD of the HSLA-420 steel.

Furthermore, a detailed fracture surface analysis was conducted using SEM to examine the failure mechanisms across different sheet directions. In general, the steel exhibited ductile fracture behaviour in all three directions, characterized by the coalescence of micro-voids. Micro-void nucleation typically occurs through mechanisms such as the cracking of precipitate particles or the failure of the particle-matrix interface [13].

Figs. 7a and 7b illustrate the fracture surfaces of samples tested along the RD and TD directions, respectively. The small equiaxed dimples within the ferrite grains indicate a ductile fracture, whereas the pearlite phase exhibits a cleavage fracture mode, as highlighted by arrows in Figs. 7a-b. This suggests that the mechanical response of each phase differs under tensile loading, with ferrite deforming plastically and pearlite failing through brittle mechanisms. Furthermore, Fig. 7a reveals an intergranular microcrack (marked by a dotted line) produced by the coalescence of micro-voids. According to Vermeij et al. [14], such voids originate from interface decohesion between ferrite (the soft phase) and pearlite (the hard phase), a phenomenon associated with stress accumulation around ferrite grains [15].

Additionally, Tsuchida et al. [16] reported that pearlite in ferrite-pearlite steels undergoes significant elongation along the tensile axis, mainly when the ferrite grain size is finer. Consistently, Figs. 7c-d show elongated pearlite grains, supporting the idea that a refined pearlite structure enhances plastic deformation capacity in low-carbon ferrite-pearlite steels. This suggests that controlling pearlite morphology could be a key factor in optimizing the ductility and toughness of HSLA steels.

Regarding samples tested along the DD direction, the fracture surface closely resembles that of RD and TD samples, confirming that the dominant failure mechanisms remain consistent.

Fatigue behaviour of HSLA-420 steel

Fig. 8 illustrates the fatigue behaviour by presenting the variation of stress amplitude as a function of the number of cycles for three imposed plastic strain ranges, namely $\Delta\varepsilon_p$ = 0.1%, 0.2%, and 0.3%, tested in RD, TD, and DD directions.

At $\Delta\varepsilon_p$ = 0.1% (Fig. 8a), the DD sample exhibits the highest stress amplitude throughout the fatigue life, whereas the TD sample shows the lowest values. The DD sample undergoes an initial hardening of approximately 3% in the second cycle, followed by gradual softening. In contrast, RD and TD samples exhibit continuous softening behaviour until failure. Notably, from the third cycle onwards, the softening slope of the RD and DD samples becomes similar.

At $\Delta\varepsilon_p$ = 0.2% (Fig. 8b), cyclic softening predominates in all three samples. The TD sample, however, maintains the lowest stress amplitude values compared to RD and DD samples.

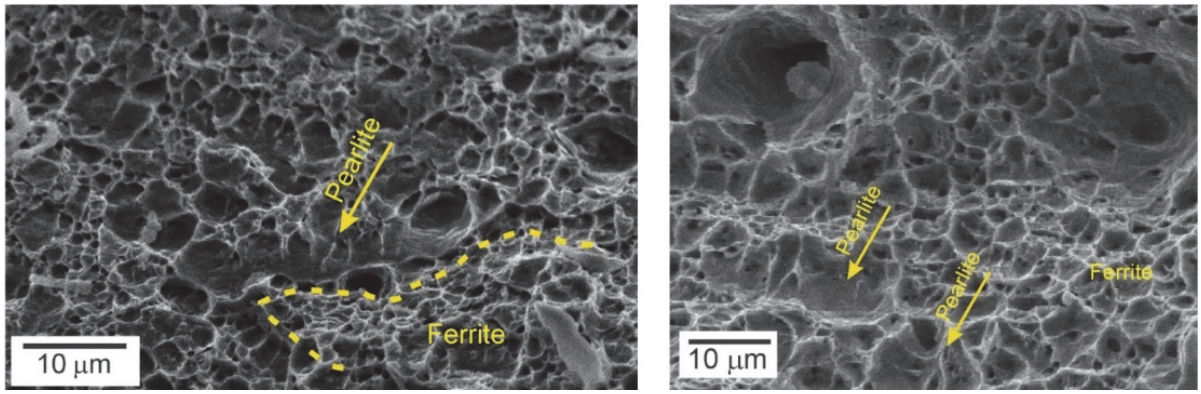

(a) (b)

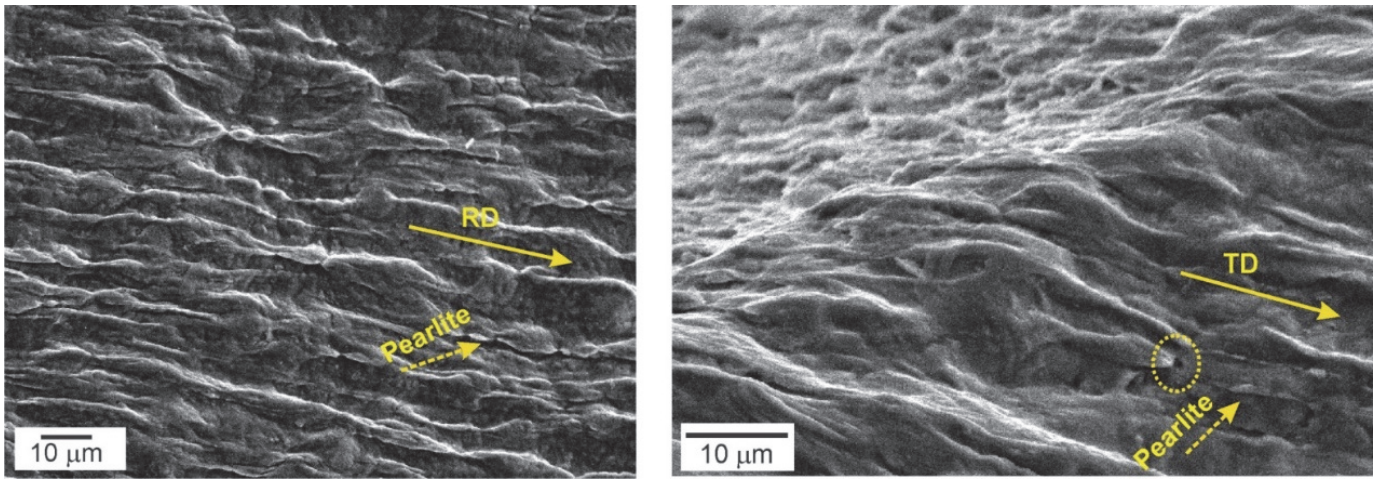

(c) (d)

Figure 7: SEM micrographs of the fracture surface: (a) RD, (b) TD. Elongation of microstructural constituents along the tensile axis: (c) RD sample, showing elongated pearlite and ferrite; (d) TD sample, highlighting a micro-void at the ferrite-pearlite interface (indicated by the circle).

At $\Delta\varepsilon_p$ = 0.3% (Fig. 8c), the RD and DD samples show continuous cyclic softening throughout their fatigue life. In contrast, the TD sample initially undergoes hardening of approximately 4%, followed by subsequent softening. Interestingly, the TD sample exhibits the highest stress amplitudes during the first 400 cycles. Between 3 and 400 cycles, the softening slopes for RD and TD are identical, while for RD and DD, the softening slopes become similar after 70 cycles.

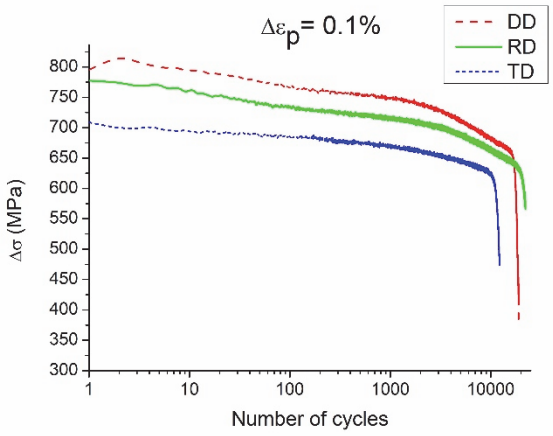

(a)

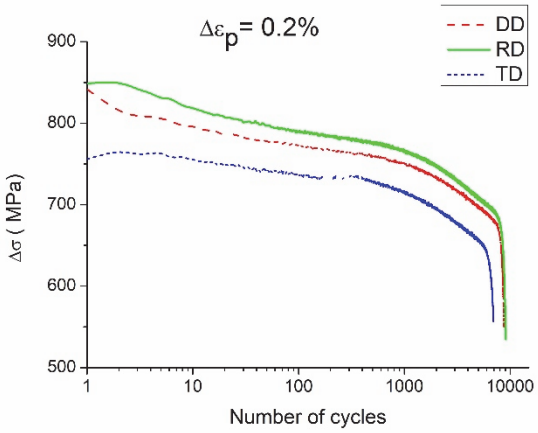

(b)

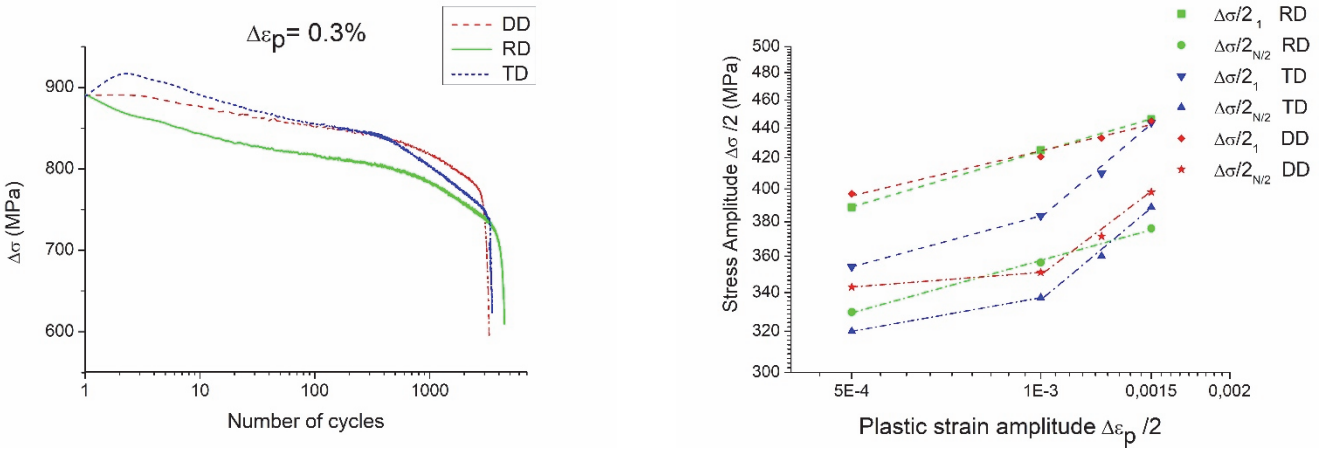

(c) (d)

Figure 8: Fatigue behaviour at different plastic strain ranges. (a) $\Delta\varepsilon_p$ = 0.1%, (b) $\Delta\varepsilon_p$ = 0.2%, (c) $\Delta\varepsilon_p$ = 0.3%; (d) CSS curve at 1st cycle and half-life (N/2) for RD, TD and DD.

To evaluate the cyclic softening at a given plastic strain amplitude, the softening ratio (δ_R) was determined using

$$\delta_R = \frac{\sigma_{max} - \sigma_{N/2}}{\sigma_{max}} \tag{3}$$

where σ_{max} and $\sigma_{N/2}$ correspond to the maximum stress amplitude and stress amplitude at the half-life, respectively. The results are summarized in Tab. 3.

Sample	δ_R at $\Delta\varepsilon_p$ = 0.1%	δ_R at $\Delta\varepsilon_p$ = 0.2%	δ_R at $\Delta\varepsilon_p$ = 0.3%
DD	0.16	0.16	0.10
RD	0.15	0.16	0.16
TD	0.10	0.12	0.16

Table 3: Softening ratio δ_R at different plastic deformation of HSLA-420 steel in the three directions of the sheet.

At $\Delta\varepsilon_p \leq 0.2\%$ the RD and DD samples exhibit a similar cyclic softening ratio. This suggests that the microstructural mechanisms driving the softening such as the accumulation and rearrangement of dislocations are comparable in these directions, with minor differences possibly attributable to slight variations in morphologic and/or crystallographic texture. However, at higher plastic strain ($\Delta\varepsilon_p$ = 0.3%), the cyclic softening ratio decreases for the DD sample but remains consistent for RD. On the other hand, TD samples at $\Delta\varepsilon_p \leq 0.2\%$ show a lower cyclic softening ratio than RD and DD samples. However, for high strains, the cyclic softening ratio is similar to RD.

Sample	n (1st cycle)	n' (N/2 cycle)
RD	0.12	0.12
DD	0.10	n_1'= 0.033 $\Delta\varepsilon_p$< 0.2% n_2'= 0.31 $\Delta\varepsilon_p$ > 0.2%
TD	n_1= 0.12 $\Delta\varepsilon_p$< 0.2% n_2= 0.36 $\Delta\varepsilon_p$ > 0.2%	n_1'= 0.076 $\Delta\varepsilon_p$< 0.2% n_2'= 0.35 $\Delta\varepsilon_p$ > 0.2%

Table 4: Strain hardening exponent (n) and cyclic strain hardening exponent at half-life (n').

On the other hand, to provide a more comprehensive characterization of cyclic behaviour, multiple tests at different strain amplitudes are performed to determine the cyclic stress-strain (CSS) curve. This curve describes the relationship between the stabilized plastic strain and the maximum stress reached in the steady-state fatigue regime. It is typically expressed using a Ramberg-Osgood-type equation

$$\frac{\Delta\sigma}{2} = K'\left(\frac{\Delta\varepsilon_P}{2}\right)^{n'} \quad (4)$$

where K' and n' are the cyclic strain hardening coefficient and exponent, respectively.
In this study, for HSLA-420 steel, the cyclic strain hardening exponent was estimated from the stress amplitude versus plastic strain curve shown in Fig. 8d. These values were then compared with the monotonic strain hardening exponent (n), which was obtained by plotting the stresses from the first cycle against the corresponding plastic strain. A summary of the results is presented in Tab. 4.
For the RD sample, n y n' have the same value. This suggests the material hardens similarly under monotonic (tensile) and cyclic deformation. In contrast, the DD samples show a strain hardening exponent n = 0.10 at the beginning of the fatigue life. However, at half-life, two distinct stages can be observed, represented by two straight lines with different slopes: n_1' = 0.033 at low plastic strain ($\Delta\varepsilon_p < 0.2\%$) and n_2' = 0.31 for larger plastic strains ($\Delta\varepsilon_p > 0.2\%$). This indicates that the material in the DD direction at low plastic strain shows limited cyclic strain-hardening capability, which can be attributed to restricted dislocation motion. However, it is more sensitive to larger deformations, which may result in enhanced strain hardening due to dislocation accumulation and other microstructural changes at higher strain levels [17,18].
Additionally, the TD sample also shows differences between low and high plastic strain ranges, with a notable change in the strain hardening exponent. In the first cycle, n_1= 0.12 for $\Delta\varepsilon_p < 0.2\%$, while n_2 = 0.36 for $\Delta\varepsilon_p > 0.2\%$, indicating a significant increase in strain hardening with higher plastic strain. Moreover, at half-life it shows a decrease in the strain hardening exponent to n_1' = 0.076 for low plastic strain ($\Delta\varepsilon_p < 0.2\%$), suggesting that the material may be undergoing stabilization or partial relaxation of strain hardening. However, for larger plastic strains, the difference between n_2 and n_2' is very low. This indicates that the cyclic strain hardening behaviour is similar to that observed during monotonic loading, where dislocation-dislocation and dislocation-precipitate interactions contribute similarly to material strengthening.
The double n' behaviour, reflecting two-stage cyclic hardening, has been previously reported for dual-phase steels with a ferrite–martensite microstructure [17], where it was attributed to the inhomogeneous distribution of the hard martensitic phase. In such systems, the pronounced contrast in hardness between ferrite and martensite induces strong local strain partitioning, promoting early transitions in strain-hardening behaviour. A similar double n' response was also reported by Majumdar et al. [18,19] in hot-rolled Ti-Mo low-carbon steels, where strengthening arises from Ti-Mo-C precipitates randomly distributed along grain boundaries and within the ferritic matrix. In that case, the double n' behaviour was linked to the evolution and rearrangement of dislocations interacting with nanoscale precipitates. Additionally, the authors reported that the change in n' was closely associated with a transition in the fatigue life behaviour, as reflected by a bilinear C-M relationship.
In the present study, the TD and DD directions of the HSLA-420 steel also exhibit a comparable double n' behaviour, suggesting analogous underlying mechanisms. However, the steel investigated here has a ferrite-pearlite microstructure without a separate hard phase such as martensite. Thus, the transition in cyclic strain-hardening may arise from interactions between dislocations and dispersed cementite particles, particularly those located at grain boundaries.
To complement the CSS curve analysis, Vickers microhardness measurements were performed on the surface of the fatigued specimens at the end of life (Nf). The measurements were taken at the central gauge section of RD, TD and DD specimens tested at different plastic strain amplitudes. As summarised in Tab. 5, hardness increased with increasing plastic strain amplitude in all orientations, reflecting strain hardening associated with dislocation accumulation and rearrangement during cycling. The effect was particularly pronounced at $\Delta\varepsilon_p$ = 0.3%, where TD and DD specimens reached an average of 217 HV and 200 HV respectively, compared to 186 HV in RD.

$\Delta\varepsilon_p$ (%)	RD (HV)	TD (HV)	DD (HV)
0.1	173	190	178
0.2	180	198	190
0.3	186	217	200

Table 5: Microhardness at the end of the fatigue life.

Furthermore, to evaluate the impact of this cyclic strain-hardening transition on fatigue life, the following section presents a detailed analysis of the Coffin-Manson relationship in the three principal directions.

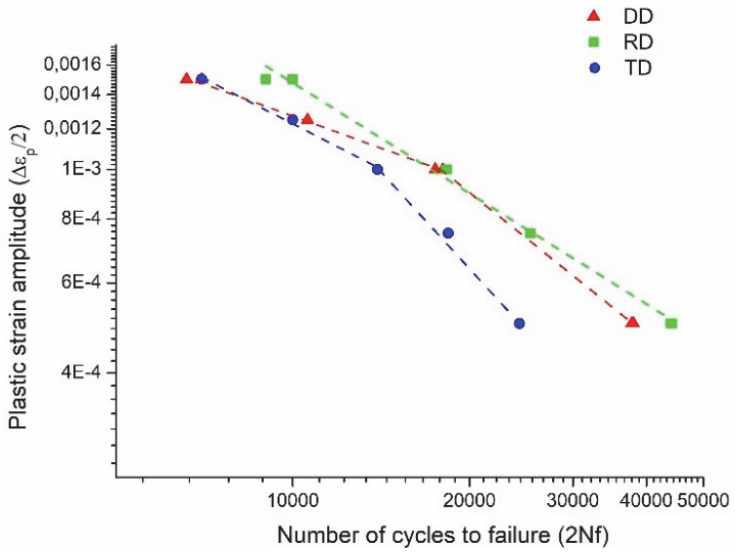

Figure 9: Coffin - Manson curve of HSLA-420 steel in DD, RD and TD directions of the sheet.

For establishing the C-M relationship between plastic strain amplitude and fatigue life of HSLA-420 steel in the three sheet directions, fatigue tests were carried out at various plastic strain ranges: $\Delta\varepsilon_p$ = 0.1%, 0.15%, 0.2%, 0.25%, and 0.3%. As shown in Fig. 9, specimens tested along the transverse direction (TD) consistently exhibit the shortest fatigue life across all strain levels. At low plastic strain amplitude ($\Delta\varepsilon_p$ = 0.1%), the fatigue life in the rolling direction (RD) is nearly twice that of TD, while at high amplitude ($\Delta\varepsilon_p$ = 0.3%), RD still outperforms TD by over 25%. Interestingly, diagonal direction (DD) samples display fatigue life comparable to RD at low strain amplitudes, but their response shifts closer to TD at higher strain levels.

Furthermore, the C-M response displays a bilinear trend in TD and DD samples, with a transition in slope occurring at $\Delta\varepsilon_p/2 = 1 \times 10^{-3}$, which coincides with the change in n' observed in Fig. 8d. In contrast, RD samples maintain a linear C-M relationship across all strain amplitudes and show no evidence of a change in n'. This directional dependence introduces a key distinction from previous studies where bilinearity and double n' behaviour were attributed to the presence of a hard phase inducing local strain heterogeneities [17]. In the present work, however, the absence of bilinearity in the RD direction of HSLA-420 suggests that phase contrast is not the dominant factor in this material. Instead, the observed behaviour is likely governed by alternative mechanisms, particularly dislocation–dislocation and dislocation–precipitate interactions. To elucidate these mechanisms and support the interpretation of the macroscopic fatigue response, dislocation structures at the end of fatigue life in all three loading directions were examined using TEM.

Dislocation structures in RD samples

At $\Delta\varepsilon_p$ = 0.1% for RD samples, a heterogeneous distribution of dislocations is observed within the ferrite grains. In Fig. 10a, the microstructure shows dislocation tangles (indicated by arrows) and wall-like arrangements (enclosed by a dotted line), similar to those found in the as-received condition. Moreover, in Fig. 10b, slip bands with a spacing of approximately 0.5-0.7 μm can be seen crossing adjacent grains, indicating early plastic activity.

At $\Delta\varepsilon_p$ = 0.2%, the dislocation structure within the ferrite grains predominantly features well-defined dislocation walls, as illustrated in Fig. 10c. In some grains, these dislocation walls subdivide the ferrite into subgrains with curved boundaries, as indicated by arrows in Fig. 10c. This observation is consistent with previous findings reported in [19]. However, it is worth noting that at this stage, the formation of subgrains remains sparse and incomplete, with subgrains only partially delineated by loosely organized dislocation walls or sub-boundaries. On the other hand, in the pearlitic regions, the microstructure exhibits no significant changes compared to the as-received condition (Fig. 10d, grain 1). Nevertheless, areas containing dispersed cementite particles show evidence of dislocation pinning, as highlighted in grain 2 of Fig. 10d. This pinning effect indicates localized interactions between dislocations and cementite.

At $\Delta\varepsilon_p$ = 0.3%, a well-defined cell structure is developed (Fig. 10e), indicating typical dynamic recovery processes during cyclic loading. Furthermore, 0.16-0.4 μm wide cells are observed between dislocation channels of 0.6-0.7 μm. The cells are mostly elongated as reported by other authors [6,19], and their interiors are free of dislocations. It is worth highlighting the fine precipitates on cell boundaries in Fig. 10f, indicating interaction dislocation-precipitates.

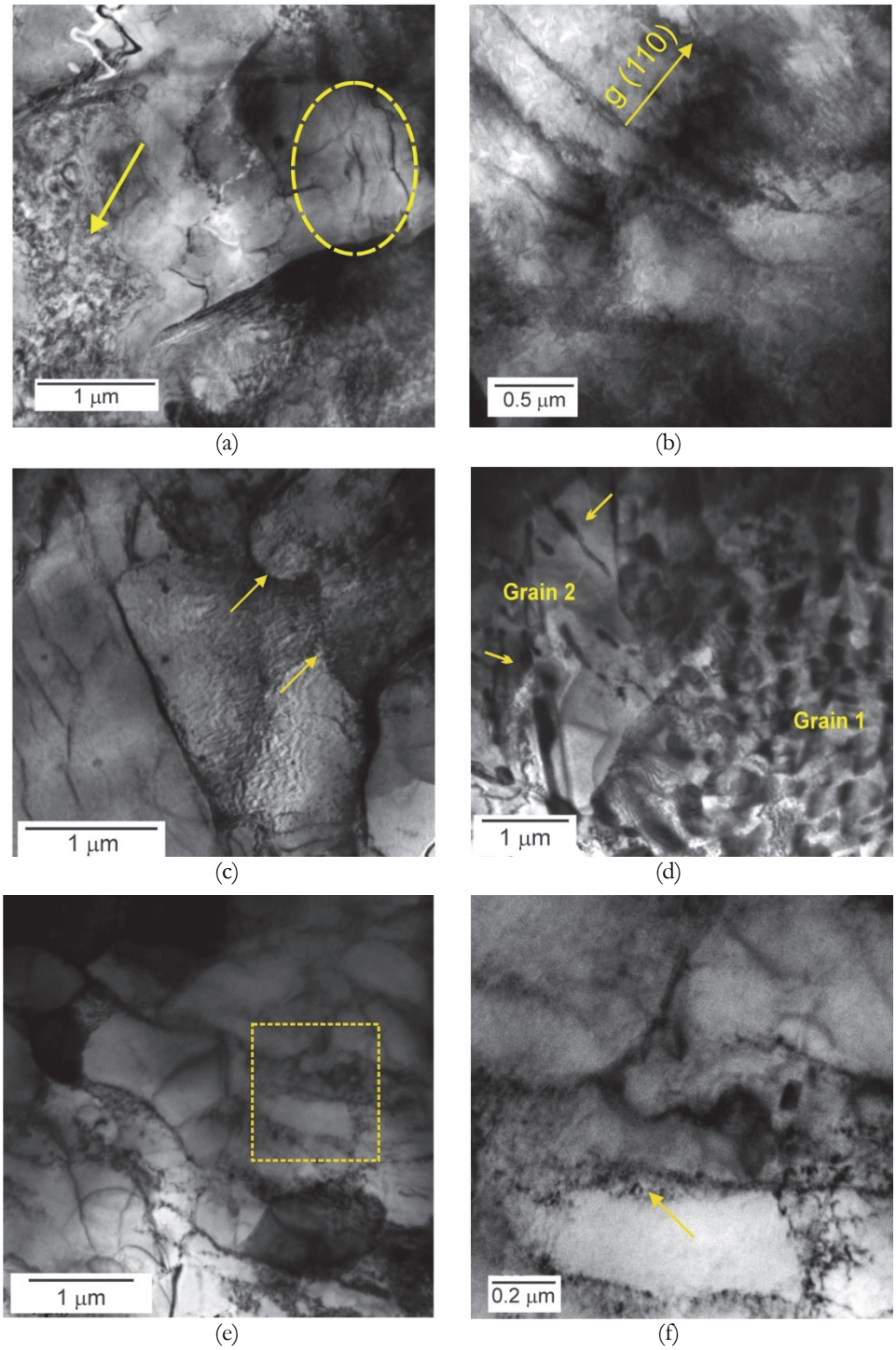

Figure 10: TEM BF microstructure showing dislocation structure of RD samples; zone axis B $[\bar{1}11]$. BCC: (a) dislocation tangles and wall-like structures at $\Delta\varepsilon_p = 0.1\%$; (b) slip bands extending across adjacent grains at $\Delta\varepsilon_p = 0.1\%$; (c) development of well-defined dislocation walls and subgrain formation with curved boundaries indicated by arrows at $\Delta\varepsilon_p = 0.2\%$; (d) dislocation pinning by cementite particles at $\Delta\varepsilon_p = 0.2\%$; (e) formation of elongated dislocation cells at $\Delta\varepsilon_p = 0.3\%$; (f) detail of dislocation cell boundaries with fine precipitates at $\Delta\varepsilon_p = 0.3\%$.

Dislocation structures in DD samples

At $\Delta\varepsilon_p = 0.1\%$, the dislocation structures in DD samples (Fig. 11a) closely resemble those observed in RD samples. However, dense dislocation accumulations are observed at specific ferrite grain boundaries. Within the ferrite grains,

dislocation walls delineate narrow channels that are largely free of dislocations, with typical widths ranging from 0.13 to 0.26 μm. These features indicate the early formation of dislocation channels bounded by wall-like arrangements. Notably, dislocation motion remains confined within individual grains and does not extend across grain boundaries, underscoring the role of grain boundary characteristics in impeding slip transmission.

At $\Delta\varepsilon_p$ = 0.2%, well-formed dislocation walls and cells are a characteristic feature (Fig. 11b). Within some ferrite grains, subgrains with widths ranging from 0.5 μm to 1 μm are observed, along with fine dislocation cells measuring 0.15-0.4 μm. These structures are frequently found near grain boundaries, which suggest that strain accumulation is localized.

At $\Delta\varepsilon_p$ = 0.3%, the dislocation substructure is dominated by subgrains, varying in size between 0.4-2 μm. These are defined by well-formed subgrain boundaries, as shown in Fig. 11c. Most of these subgrains exhibit dislocation-free interiors, while a few contain dislocation cells approximately 0.1-0.3 μm in size. Precipitates along the grain boundaries play a critical role, serving as barriers to dislocation motion and contributing to strain localization and stress concentration. These interactions between dislocations and precipitates significantly influence the microstructural evolution under cyclic loading.

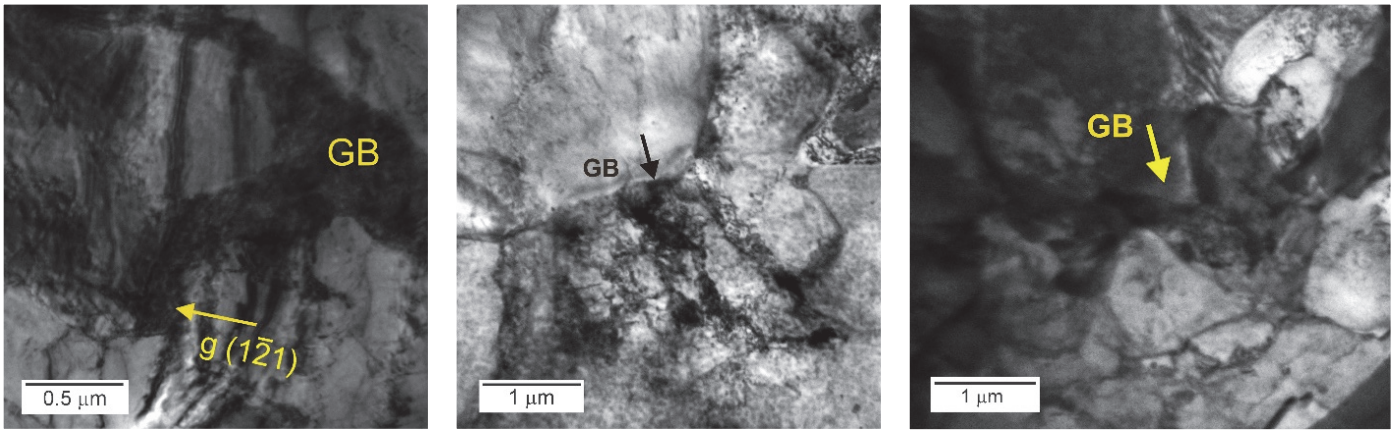

(a) (b) (c)

Figure 11: TEM BF micrograph showing dislocation substructure of DD samples: (a) at $\Delta\varepsilon_p$ = 0.1%, dislocation walls and dense dislocations in grain boundary (GB); zone axis B$[012]$ BCC; (b) at $\Delta\varepsilon_p$ = 0.2%, well-developed dislocation walls and early-stage subgrain structures localized near grain boundaries; (c) at $\Delta\varepsilon_p$ = 0.3%, well-defined subgrains and dislocation–precipitate interaction.

Dislocation structures in TD samples

At low plastic strain levels ($\Delta\varepsilon_p \leq$ 0.2%), the dislocation structure in TD samples is characterized by a non-uniform distribution of dislocations within the ferrite grains (Figs. 12a and b). This distribution includes dislocation tangles, vein-like formations and well-defined dislocation walls. Planar dislocation arrays and dislocation cells are observed within dislocation channels ranging from 1-2 μm in width. Inside these channels, the dislocation cells measure between 0.1 and 0.2 μm, as shown in Fig. 12b. Notably, Fig. 12c shows the formation of subgrains from a grain boundary, where dislocation walls intersect and define localized zones of strain accommodation. In the pearlitic regions, dislocations within the ferrite are confined by cementite precipitates, as shown in Fig. 12d.

At higher plastic strain ($\Delta\varepsilon_p$ = 0.3%), subgrains become the dominant dislocation substructure. These subgrains range from 0.5 to 2 μm in size and display high internal dislocation densities organized into veins and cells, as highlighted in Figs. 13a and 13b. A pronounced accumulation of dislocations is observed along the grain boundary shown in Fig. 13c. This localized build-up of dislocations indicates a significant barrier to slip transmission across the grain boundary, which in turn leads to stress concentration in its vicinity. Such heterogeneities in the dislocation structure are known to promote the nucleation of microcracks under cyclic load, highlighting the critical role of grain boundary strength [8].

The pearlitic regions in the TD samples (Fig. 13d) exhibit a higher density of dislocations confined by thick cementite lamellae (approximately 0.15 μm). This restriction of dislocation mobility further contributes to localized stress concentration and the initiation of fatigue cracks. According to Korda et al. [20], the observed subgrain formation, coupled with stress localization at cementite precipitates and grain boundaries, is a key factor in the accelerated fatigue crack propagation and reduced fatigue life.

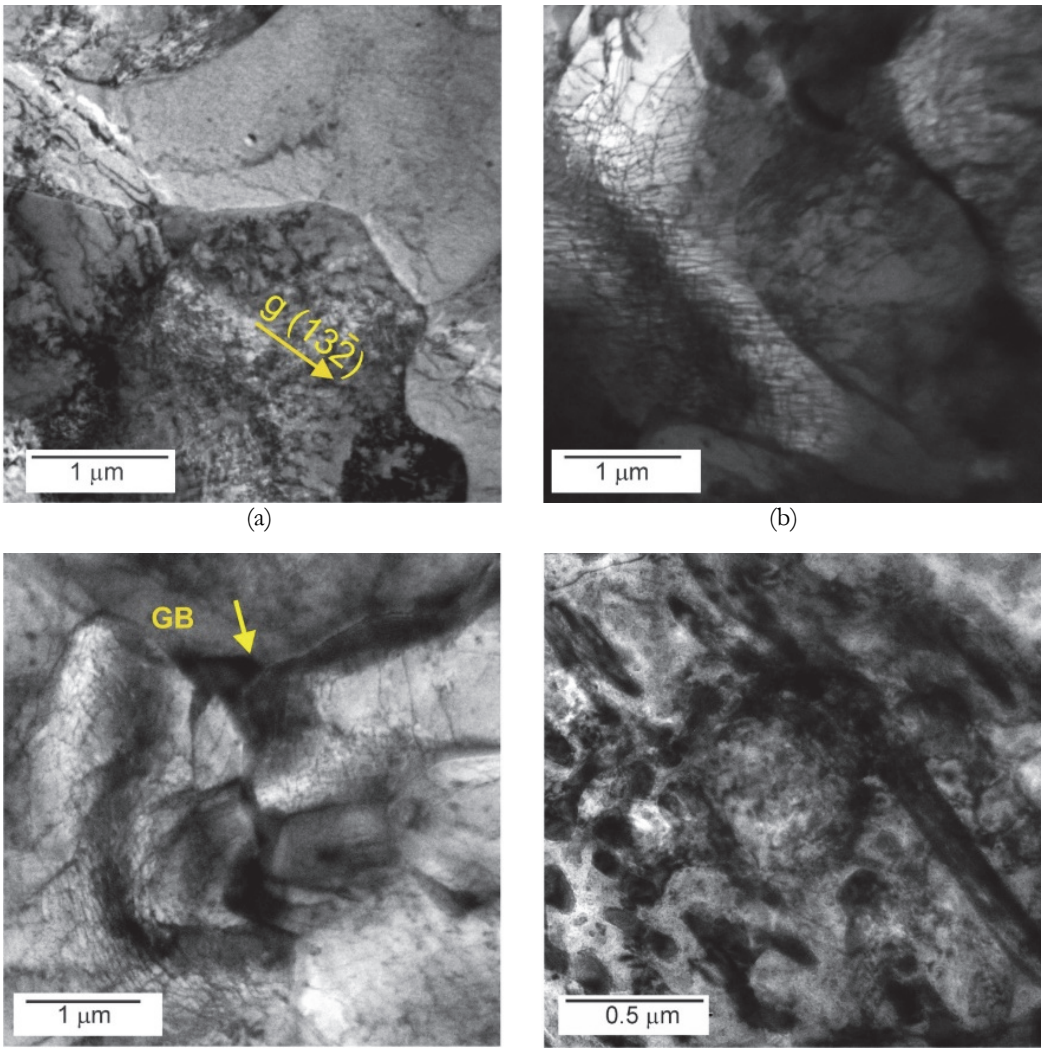

Figure 12: TEM BF micrograph showing dislocation substructures in TD samples fatigued at $\Delta\varepsilon_p = 0.1\%$: (a) Zone axis B$[023]$ BCC. Non-uniform dislocation distribution in ferrite, including dislocation tangles and vein-like formations; (b) dislocation cells within channels, (c) subgrain formation initiated at grain boundary, (d) dislocations confined by cementite within pearlite colonies.

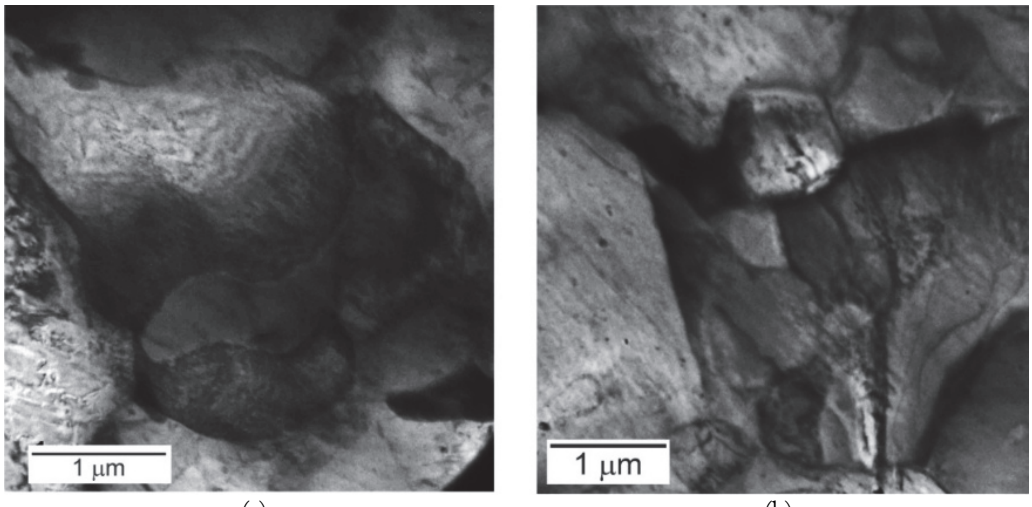

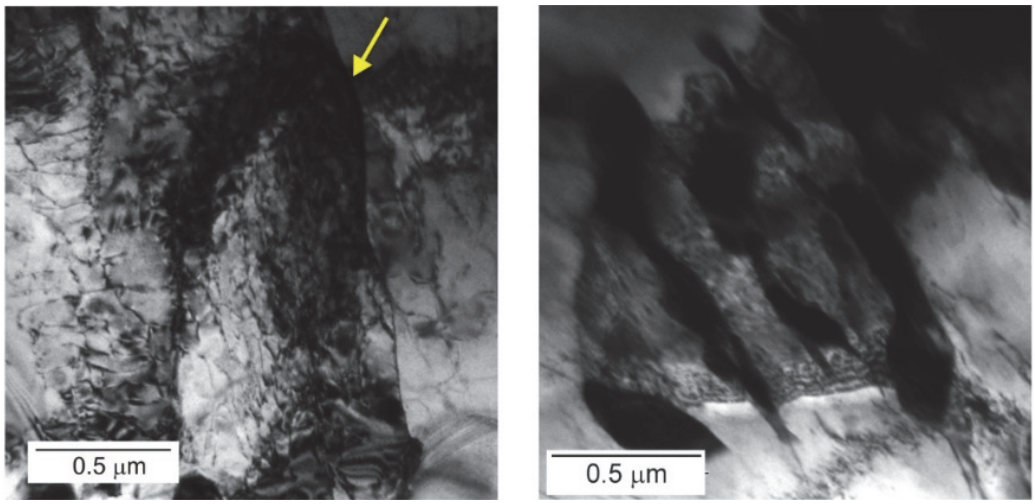

(c) (d)

Figure 13: TEM BF micrograph showing dislocation substructures in TD samples fatigued at $\Delta\varepsilon_p$ = 0.3%: (a) vein structure within subgrains; (b) cell structures within subgrain; (c) high dislocation concentration at grain boundaries (indicated by arrows); (d) dense dislocation networks confined by thick cementite lamellae within pearlite colonies.

Fatigue cracks in RD and TD samples

Fig. 14 presents the morphology of microcracks observed in RD and TD samples under plastic strains of $\Delta\varepsilon_p$ = 0.1% and 0.3%, at the end of fatigue life. At low plastic strain ($\Delta\varepsilon_p$ = 0.1%), the RD samples exhibit a high density of microcracks that initiate predominantly within ferrite grains, as shown in Fig. 14a (highlighted by dotted lines). According to TEM observations, these sites coincide with the presence of slip bands (Fig. 10b), suggesting that intragranular cracking is associated with early plastic activity localized in these bands. This is consistent with the findings of Das Bakshi et al. [21], who reported the activation of favourable slip systems (e.g. {110}⟨111⟩) enables intragranular plastic deformation, delaying fatigue damage accumulation at grain boundaries. Some cracks propagate toward adjacent grains (e.g., crack F1 in Fig. 14a). Other cracks are arrested at grain boundaries (e.g., F2 in the same figure), indicating that grain boundaries in this orientation act as effective barriers to crack propagation. Additionally, some cracks nucleate directly at grain boundaries (indicated by arrows in Fig. 14a), although most remain short and do not propagate significantly.

In contrast, TD samples exhibit dominant crack initiation at grain boundaries, as shown in Fig. 14c. This observation is consistent with dislocation accumulation and compact subgrain formation near grain boundaries (Fig. 12c), which promotes local stress concentration and intergranular crack initiation. These observations agree with studies by Chen et al. [22] who reported that high geometrically necessary dislocation (GND) density and local misorientations at grain boundaries drive strain localization and early crack nucleation.

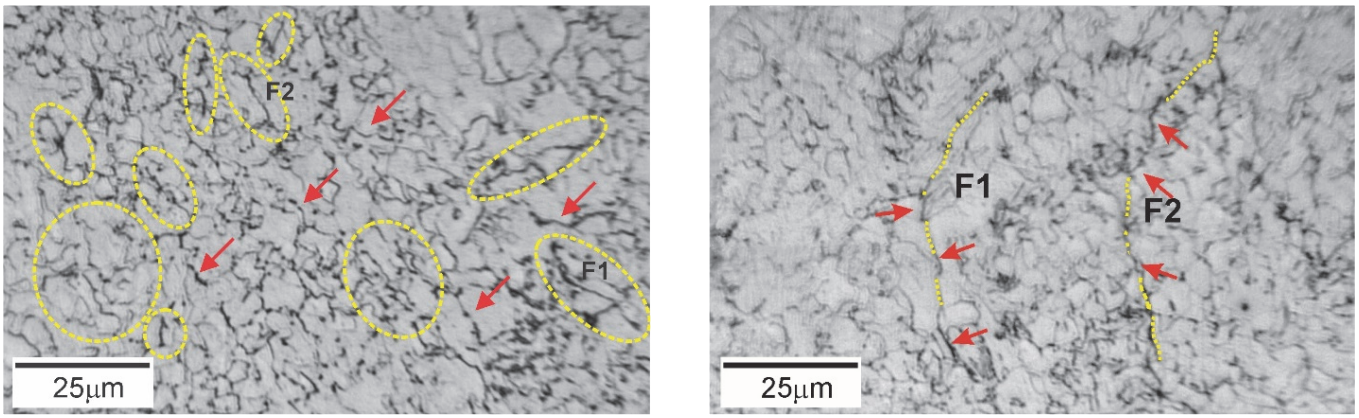

(a) (b)

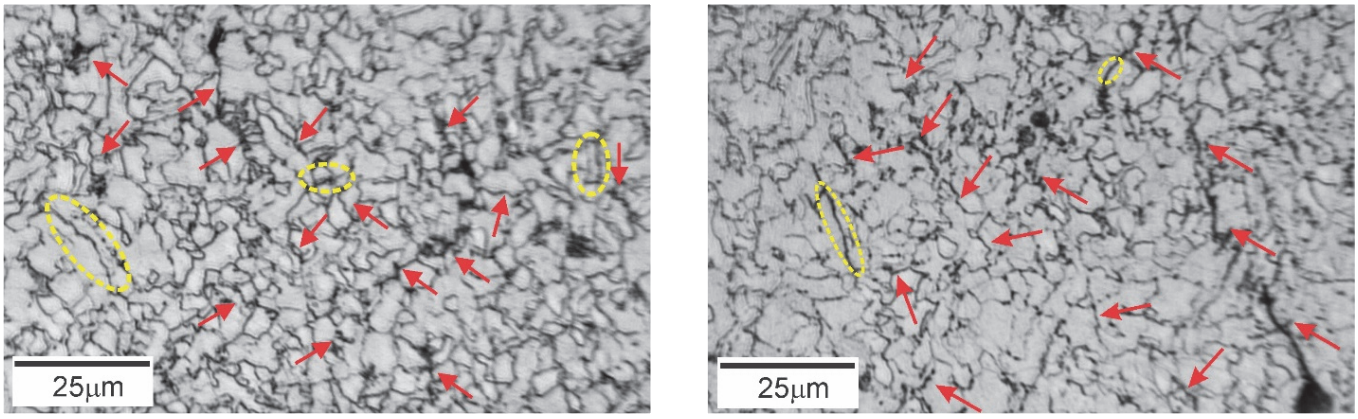

(c) (d)

Figure 14: Optical micrograph of microcracks at the end of the fatigue life, (yellow circle: trasgranular cracks, red arrow: intergranular cracks): (a) RD at $\Delta\varepsilon_p = 0.1\%$; (b) RD at $\Delta\varepsilon_p = 0.3\%$ (yellow dots: transgranular cracks), (c) TD at $\Delta\varepsilon_p = 0.1\%$, (d) TD at $\Delta\varepsilon_p = 0.3\%$.

On the other hand, Fig. 15 shows the distribution of crack lengths measured using ImageJ software from 20 optical micrographs for each sample. Comparing RD and TD (Figs. 15a and 15c), a higher total crack density is observed in TD (4.7×10^8 m^{-2}) compared to RD (3×10^8 m^{-2}). In both cases, most cracks fall within the 6-12 μm range, with similar counts (~110 cracks). However, TD samples exhibit more cracks exceeding 12 μm, indicating that crack propagation is more critical in TD.

These microstructural observations explain the reduced fatigue life of TD samples compared to RD at low plastic strain amplitudes. In RD, intragranular crack initiation and effective grain boundary crack arrest delay fatigue failure, whereas in TD, the predominance of intergranular cracking, higher crack density, and early crack growth accelerate damage accumulation and reduce fatigue life.

At higher plastic strain ($\Delta\varepsilon_p = 0.3\%$), RD samples show a lower crack density (3.7×10^8 m^{-2}) compared to TD samples (5×10^8 m^{-2}). In the RD samples, cracks propagate in a mixed mode -both transgranular and intergranular- as seen in Fig. 14b (cracks F1 and F2). In contrast, cracks in TD samples predominantly follow grain boundaries (Fig. 14d), indicating a more pronounced intergranular fracture mode. A direct comparison between Figs. 15b and 15d reveals that RD samples retain a higher number of small cracks confined within individual grains (i.e., less than 6 μm) than those in TD samples. This observation aligns with the findings of Lu et al. [23], who demonstrated that the formation of subgrains under cyclic loading accelerates fatigue crack propagation by promoting slip incompatibility and stress concentration along sub-boundaries. Similarly, Zhao et al. [24] emphasized that subgrains formed during LCF in ferritic alloys correlate with a shift from crack initiation to propagation-controlled fatigue. These mechanisms are clearly manifested in the TD samples analysed here. In particular, Fig. 16 reveals a microcrack propagating through a region of aligned subgrains, highlighted with red dashed lines. These subgrains correlate with the structures previously identified via TEM in Figs. 13a-c, confirming that the presence of compact subgrain structures and localized plasticity at grain boundaries promotes intergranular crack propagation under cyclic loading.

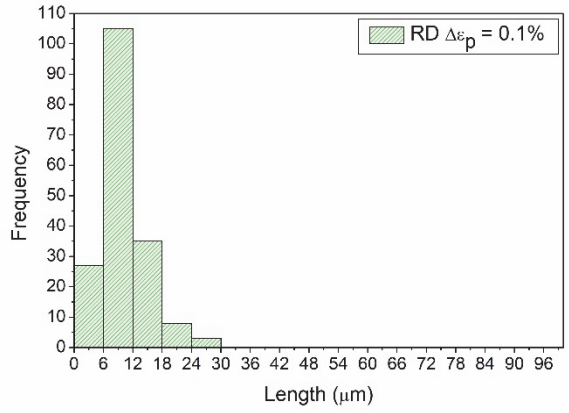

(a)

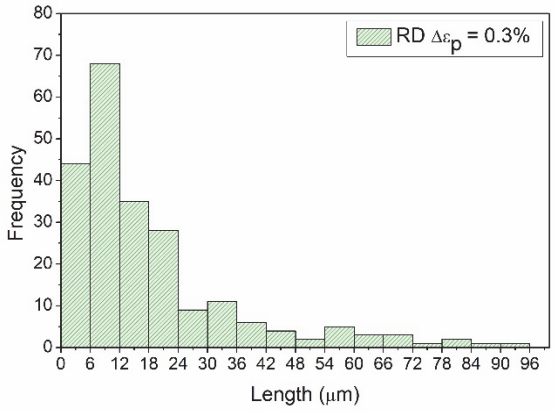

(b)

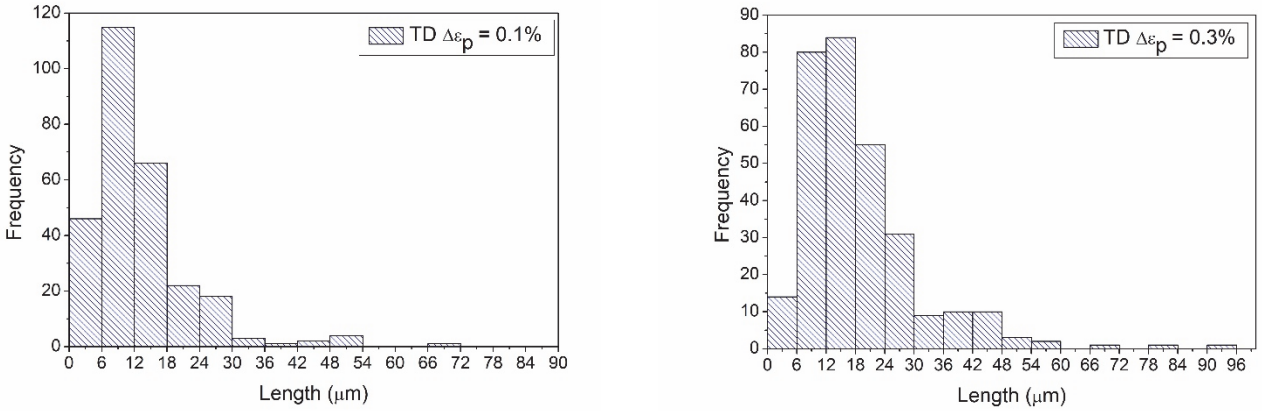

Figure 15: Distribution of crack lengths taken from 20 optical micrographs: RD samples at (a) $\Delta\varepsilon_p$ = 0.1%, (b) $\Delta\varepsilon_p$ = 0.3%, TD samples at (c) $\Delta\varepsilon_p$ = 0.1%, (d) $\Delta\varepsilon_p$ = 0.3%.

Although no significant changes were observed in the pearlite structure, it is well-established that pearlite can slow down crack growth [11,13]. Wang et al. [25] reported that cementite particles within pearlite colonies play a crucial role in hindering dislocation motion and trapping a significant number of dislocations within the grain interiors as observed in the present work in Figs. 12d and 13d. Owing to the dislocations are effectively immobilized by the cementite particles, yield strength and work hardening will increase. In contrast, intergranular cementite particles are in fractional positions along the grain boundaries (as shown in Figs. 12c and 13c). This reduces the dislocation accumulation capacity at the grain boundaries, weakening their overall strength. Consequently, the intergranular cementite particles can impair the ability of the grain boundaries to resist stress, potentially promoting crack initiation under cyclic loading.

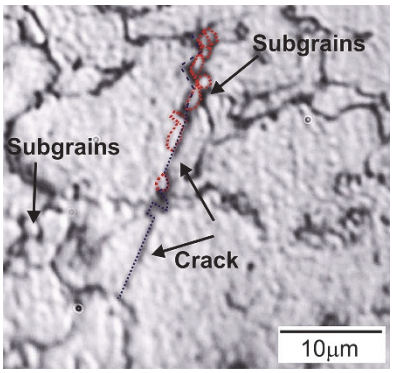

Figure 16: Optical micrograph of TD sample at $\Delta\varepsilon_p$ = 0.3% showing intergranular crack propagation through a region of aligned subgrains, highlighted with red dashed lines.

Relation between fatigue behaviour and dislocation structure

The progression of cyclic plastic deformation and the resulting mechanical properties in metallic materials are fundamentally driven by the evolution of dislocation structures [5,6]. This study aims to interpret the cyclic behaviour of HSLA-420 steel by examining the dislocation structure transformations occurring during low-cycle fatigue. The findings reveal that key aspects, such as the cyclic stress response, the nature of cyclic softening and changes in hardening factors, can be directly linked to the diverse dislocation structures observed at different levels of plastic strain.

The cyclic behaviour observed for the plastic strain ranges ($\Delta\varepsilon_p \leq 0.3\%$) in the three principal directions of the HSLA-420 sheet predominantly exhibits cyclic softening (Fig. 8a-c). Previous studies have identified two cyclic responses (softening or hardening) depending on the imposed strain range in microalloyed ferritic-pearlitic steels. For instance, Sankaran et al. [11], in a medium-carbon steel, reported cyclic softening up to a total strain of 0.7%, transitioning to hardening at higher strains. Similarly, Roven et al. [6] documented a comparable trend in low-carbon offshore steel with low pearlite content, reporting cyclic softening up to a plastic strain range of 0.7%, followed by hardening at higher plastic strain levels. The authors indicated that the transition value depends strongly on the accumulated plastic strain. Fredriksson et al. [4]

observed cyclic softening at total strain amplitudes below 0.8% in a low-carbon, cold-rolled HSLA-500 steel with a low pearlite fraction. Overall, the authors attributed these behaviours to the evolution of the dislocation substructure in the ferritic phase.

The HSLA-420 steel in the as-received condition exhibits a high dislocation density (~ 4 x 10^{12} m^{-2}) as a consequence of the thermomechanical deformation introduced during hot rolling. TEM analysis reveals that dislocations are heterogeneously distributed, predominantly within the ferritic phase, where they organize into tangled networks and planar arrays resembling wall-like structures (Fig. 3a). Upon cyclic deformation, dislocation dynamics are activated through mechanisms such as cross-slip and secondary slip. Cross-slip of screw dislocations facilitates the annihilation of dislocations of opposite signs and the truncation of edge segments, giving rise to persistent slip channels (Figs. 10b and 11a) [6]. Concurrently, secondary slip contributes to the formation of high-density dislocation arrangements via multiple interactions, leading to the development of dislocation walls. These walls act as barriers that can trap mobile dislocations, further increasing local dislocation density. As cyclic strain progresses, these structures evolve into well-defined dislocation cells, as evidenced in Fig. 10e. Particularly, in RD at $\Delta\varepsilon_p$ = 0.3%, the formation of elongated, well-defined dislocation cell structures free of dislocations in their interior led to a marked reduction of 85% in dislocation density, as shown in Tab. 6. Therefore, according to [6,11,26], the progressive rearrangement of dislocations into low-energy dislocation substructures, such as walls and cells, contributes to cyclic softening.

The initial cyclic hardening observed in the DD samples at $\Delta\varepsilon_p$ = 0.1% and the TD samples at $\Delta\varepsilon_p$ = 0.3% can be attributed to the generation of mobile dislocations during cycling. These new dislocations interact with precipitates and pre-existing dislocations, thereby contributing to hardening [11,19]. In particular, in the TD sample fatigued at $\Delta\varepsilon_p$ = 0.3%, a 225% increase in dislocation density was observed, leading to higher stresses, as shown in Fig. 8c.

Conversely, the reduced softening observed in the DD samples at $\Delta\varepsilon_p$ = 0.3% (Tab. 2) can be attributed to the reorganization of dislocations into small subgrains with well-defined boundaries, as shown in Fig. 11c. These subgrains are predominantly dislocation-free in their interiors, with boundaries reinforced by cementite precipitates. This stable substructure limits further dislocation motion and accumulation, thereby reducing the extent of cyclic softening [8,27].

Although the TD samples show small subgrains similar to those in the DD samples, the subgrains in TD contain dislocation substructures, such as veins and cells (Fig. 13a-b). This ongoing dislocation rearrangement within the subgrains contributes to a less stable substructure, leading to more pronounced softening in the TD samples compared to the DD samples.

On the other hand, regarding CSS curve, Fig. 8d reveals two distinct regimes for the TD and DD directions, characterized by different cyclic strain-hardening exponents (n'). This behaviour was attributed to the evolution of dislocation substructures at several strain levels [6,18,19]. Particularly, at low plastic strain ($\Delta\varepsilon_p$ < 0.2%), dislocation tangles, walls and cell-like structures were observed (Figs. 11a and 12a-c), while at higher plastic strain ($\Delta\varepsilon_p$ > 0.2%), the formation of subgrains with well-defined boundaries (Figs. 11c and 13) plays a significant role in the intensified cyclic hardening observed at these strain levels [6].

The hardness results obtained at Nf in Tab. 5 are consistent with the cyclic strain-hardening behaviour described above. At high plastic strain ($\Delta\varepsilon_p$ = 0.3%), the TD direction exhibits the largest hardness increase (217 HV), while DD also shows significant hardening (200 HV), both exceeding that of RD (186 HV). This hierarchy (TD > DD > RD) aligns with the increase in n' for TD and DD above 0.2% and supports the conclusion that TD and DD samples experience more intense substructure evolution at high strain amplitudes, as discussed in the TEM analysis.

To better understand the change of n' at low and high plastic strain, the microstructure-based model proposed by Chauhan [28] can be applied. In this framework, the yield stress is interpreted as the combined effect of strengthening contributions according to the expression:

$$\sigma_y = \sigma_g + \sqrt{\sigma_d^{\,2} + \sigma_p^{\,2}} \tag{5}$$

where σ_g, σ_d and σ_p are the contributions from grain size or Hall-Petch strengthening, dislocation forest strengthening and nanoparticles strengthening, respectively. In the present case, the evolution of σ_g and σ_d with plastic strain provides a rational explanation for the observed behaviour. The contribution of σ_p is assumed to remain unchanged during cyclic plastic deformation and between directions, as no significant particle coarsening or redistribution was observed.

The contribution of Hall-Petch strengthening to the yield strength is estimated using Eqn. (6) [24,28]

$$\sigma_g = \frac{1}{5} G \sqrt{\frac{b}{d}} \tag{6}$$

G is the shear modulus (approximately 81 GPa at room temperature as specified in EUROCODE 3: Table of Design Material Properties), b is the Burgers vector (0.248 nm for ferrite [28]), and *d* represents the average grain size.
Dislocation forest strengthening, resulting from interactions between dislocations, is quantified using the Bailey-Hirsch relationship [28]

$$\sigma_d = \alpha_d M G b \sqrt{\rho_d} \tag{7}$$

where α_d is the dislocation interaction strength coefficient (1/3 [28]), M is the Taylor factor, generally 3 for BCC crystals, and ρ_d is the dislocation density.
The estimated values of Hall-Petch strengthening and dislocation forest strengthening are listed in Tab. 6.
For instance, TEM observations in TD samples indicate that at higher plastic strains ($\Delta\varepsilon_p > 0.2\%$), ferrite grains subdivide into subgrains of approximately 1250 nm on average, compared to the original grain size of ~5000 nm. This refinement increases the Hall-Petch contribution from ~114 MPa to ~228 MPa. Concurrently, the dislocation density rises significantly at $\Delta\varepsilon_p = 0.3\%$, enhancing the dislocation forest strengthening from ~17 MPa to ~72 MPa. Thus, both dislocation accumulation and subgrain formation, synergistically contribute to the pronounced cyclic hardening observed at higher plastic strain amplitudes. In contrast, at lower strain amplitudes, only the dislocation density changes significantly, affecting primarily the σ_d value. As a result, the strain-hardening exponents differ between low and high plastic strain amplitudes (Fig. 8d), with $n_1' < n_2'$.

Sample	$\Delta\varepsilon_p$ (%)	*d* (nm)	ρ_d (m^{-2}) at Nf	σ_g (MPa)	σ_d (MPa)
TD	0.1	5000	6.8×10^{11}	114	17
	0.3	1250	1.3×10^{13}	228	72
RD	0.1	6000	3.3×10^{12}	104	36
	0.3	6000	5.7×10^{11}	104	15

Table 6: Experimental results: grain size *d*, dislocation density ρ_d at Nf, and strengthening contributions: Hall-Petch strengthening σ_g and dislocation forest strengthening σ_d.

Bilinear Coffin–Manson curve in TD and DD specimens

Unlike RD specimens, which exhibit a linear C-M relationship across the entire plastic strain range, TD and DD specimens display a distinct bilinear trend, with a slope transition occurring near $\Delta\varepsilon_p/2 = 1 \times 10^{-3}$ (Fig. 9). While similar bilinearity has been previously reported in dual-phase steels and attributed to the contrast in mechanical properties between soft ferrite and hard martensite [18], such a phase contrast explanation does not apply here. In HSLA-420, the microstructure (comprising ferrite and pearlite) is essentially the same in RD, TD, and DD samples. Therefore, the absence of bilinearity in RD suggests that the phenomenon originates from microstructural orientation effects rather than from phase distribution.
A more consistent interpretation can be drawn from the microstructure-based fatigue model proposed by Cruzado et al. [29], who attributed the bilinear behaviour of the C-M curve to a transition in the dominant deformation mechanisms. At low plastic strain amplitudes, deformation is highly localized, limited to favourably oriented grains, and fatigue life is primarily governed by crack initiation. As the strain amplitude increases, plastic deformation becomes more homogeneously distributed across the grain population, leading to a regime where crack propagation plays a dominant role in fatigue life.
The results in this paper support this interpretation. In TD and DD specimens, low plastic strain levels promote intense strain localization near grain boundaries, where fatigue cracks preferentially initiate. However, at higher plastic strain amplitudes, a substantial evolution of the dislocation substructure occurs. TEM observations confirm the subdivision of ferrite grains into dense subgrains. This structural refinement enhances both Hall-Petch and forest dislocation strengthening, contributing to the observed cyclic hardening.

Beyond its strengthening effect, subgrain formation is also closely linked to fatigue crack propagation, as illustrated in Fig. 16. This microstructural feature promotes premature intergranular crack growth, thereby reducing fatigue life. Therefore, the bilinear behaviour observed in the C-M curves of TD and DD specimens reflects not only a transition in the strain hardening regime, evidenced by the change in n' (Fig. 8d), but also a parallel shift in the dominant fatigue damage mechanism: from crack initiation at low strain amplitudes to subgrain-driven crack propagation at higher amplitudes. These findings underscore the critical role of microstructural evolution in controlling both the mechanical response and fatigue damage in HSLA-420 steel under multiaxial loading orientations.

CONCLUSIONS

This work provided a comprehensive analysis of the low-cycle fatigue (LCF) behaviour of ferritic-pearlitic HSLA-420 steel sheets, with emphasis on the influence of loading direction on fatigue life, cyclic softening, dislocation substructures, and crack initiation and propagation mechanisms. The study combined mechanical testing and detailed microstructural characterization (OM, SEM, TEM) to establish correlations between fatigue performance and the underlying microstructural evolution across three principal orientations: rolling (RD), transverse (TD), and diagonal (DD). The main conclusions are as follows:

• Tensile behaviour: HSLA-420 steel demonstrates a favourable balance between strength and ductility. Tensile behaviour was similar across the three directions**,** consistent with the weak crystallographic texture and comparable ferrite–pearlite microstructures. All specimens exhibited ductile fracture, characterized by microvoids coalescence in ferrite and cleavage in pearlite.

• Fatigue Behaviour: cyclic softening predominates across all tested plastic strain amplitudes ($\Delta\varepsilon_p \leq 0.3\%$) and loading directions, driven by the progressive rearrangement of dislocations into low-energy substructures such as walls and cells. However, TD samples at $\Delta\varepsilon_p = 0.3\%$ initially exhibit cyclic hardening, attributed to an increase in dislocation density and the pinning effect of cementite precipitates.

• Fatigue life: fatigue life is strongly direction-dependent. RD specimens outperformed TD across all strain levels, showing nearly double the fatigue life at $\Delta\varepsilon_p = 0.1\%$ and over 25% higher life at $\Delta\varepsilon_p = 0.3\%$. DD samples exhibited similar fatigue life to RD at low strain but behaved closer to TD at higher strain levels.

• Coffin–Manson relationship: RD samples followed a linear C-M relationship, whereas TD and DD samples exhibited a bilinear trend, with a transition at $\Delta\varepsilon_p/2 = 1 \times 10^{-3}$. This inflection point reflects a change in the cyclic strain-hardening exponent, linked to the evolution of dislocation structures into well-defined subgrains within ferrite grains at higher strain levels. While this subgrain formation contributes to cyclic hardening, it also promotes intergranular crack propagation, thereby shortening the fatigue life in TD and DD samples.

• Fatigue crack: the morphology and distribution of fatigue cracks revealed distinct damage mechanisms depending on loading direction. At low plastic strain amplitudes, RD samples exhibited predominantly intragranular crack initiation within ferrite grains, often arrested at grain boundaries, whereas TD samples showed intergranular cracking associated with dislocation pile-up and subgrain formation near grain boundaries. At higher strain amplitudes, crack propagation became more critical, especially in TD, where aligned subgrains facilitated intergranular crack growth and contributed to the observed reduction in fatigue life.

• Influence of pearlite and intergranular cementite: the cementite within pearlite colonies contributes positively by helping to immobilize dislocations, thus enhancing mechanical strengthening. However, a critical and significant finding of this work is the role of intergranular cementite particles located along grain boundaries or at subgrain boundaries within ferrite grains. These particles reduce the ability of these boundaries to accumulate and reorganize dislocations, diminishing the resistance to cyclic loading and promoting early crack initiation and propagation, especially at high plastic strain amplitudes.

ACKNOWLEDGEMENTS

This work was carried out with the support of the following institutions: The National Scientific and Technical Research Council (CONICET), the Santa Fe Agency for Science, Technology, and Innovation (ASACTEI), the National University of Rosario (UNR), and the companies Máquinas Agrícolas OMBU S.A. and Remolques OMBU S.A. The authors express their sincere gratitude for their valuable contributions to this research.

REFERENCES

[1] Rana, R. and Singh S.B ed. (2017), 6 - High strength low alloyed (HSLA) steels, Woodhead Publishing, In: Automotive Steel Design, Metallurgy, Processing and Applications, Woodhead Publishing, pp. 145-167. DOI: https://doi.org/10.1016/B978-0-08-100638-2.00006-7

[2] Arman, L. and Alzari, S. (2012). Comparative fem simulation of dynamic loads on a trailer structure made of carbon manganese and microalloyed steels produced in Terniur Siderar, 6th Conference on Uses of Steel IAS, Rosario, Argentina pp. 33-44.

[3] Prosgolitis, C.G., Kermanidis, A.T., Kamoutsi, H., and Haidemenopoulos, G.N. (2022). Low Cycle Fatigue Behavior of Plastically Pre-Strained HSLA S355MC and S460MC Steels. Materials (Basel), 15(22). DOI: https://doi.org/10.3390/ma15227927.

[4] Fredriksson, K., Melander, A. and Hedman, M. (1988). Influence of prestraining and ageing on fatigue properties of high-strength sheet steels, Int. J. Fatigue 10, pp. 139–151.DOI: https://doi.org/10.1016/0142-1123(88)90056-4.

[5] Eifler, D. and Macherauch, E. (1990) Microstructure and cyclic deformation behaviour of plain carbon and low-alloyed steels, Int. J. Fatigue 12, pp. 165–174. DOI: https://doi.org/10.1016/0142-1123(90)90092-S.

[6] Roven, H.J. and Nes, E. (1991). Cyclic deformation of ferritic steel—I. Stress-strain response and structure evolution, Acta Metall. Mater., 39, pp. 1719–1733. DOI: https://doi.org/10.1016/0956-7151(91)90141-M.

[7] Milan, M. Spinelli, D. Bosefilho, W. (2001). Fatigue and monotonic properties of an interstitial free steel sheet (FMPIF), Inter. J. Fatigue 23, pp. 129–133. DOI: https://doi.org/10.1016/S0142-1123(00)00076-1.

[8] Paul, S.K. (2024). Cyclic deformation response of annealed low-carbon steel, Journal of Alloys and Metallurgical Systems 6, 100075. DOI: https://doi.org/10.1016/j.jalmes.2024.100075.

[9] de Keijser, T.H., Langford, J.I., Mittemeijer, E.J. and Vogels, A.B.P. (1982). Use of the Voigt function in a single-line method for the analysis of X-ray diffraction line broadening, J Appl Crystallogr 15, pp. 308–314. DOI: https://doi.org/10.1107/S0021889882012035.

[10] Williamson GK, Smallman RE.(1956) III. Dislocation densities in some annealed and cold-worked metals from measurements on the X-ray debye-scherrer spectrum. Philosophical Magazine, 1(1), pp. 34–46. DOI: https://doi.org/10.1080/14786435608238074.

[11] Sankaran, S., Subramanya Sarma, V., Padmanabhan, K.A. (2003). Low cycle fatigue behavior of a multiphase microalloyed medium carbon steel: Comparison between ferrite–pearlite and quenched and tempered microstructures. Mater Sci Eng. A, 345(1-2), pp. 328–335. DOI: https://doi.org/10.1016/S0921-5093(02)00511-7.

[12] Song, R., Ponge, D., Raabe, D. (2005). Mechanical properties of an ultrafine grained C–Mn steel processed by warm deformation and annealing. Acta Materialia, 53(18), pp. 4881–4892. DOI: https://doi.org/10.1016/j.actamat.2005.07.009.

[13] Gao, N., Lu, DH., Zhao, Y.Y., Liu, X.W., Liu, G.H., Wu, Y. (2019). Strengthening of a CrMnFeCoNi high-entropy alloy by carbide precipitation. Journal of Alloys and Compound, 792, pp.1028–1035. DOI: https://doi.org/10.1016/j.jallcom.2019.04.121.

[14] Vermeij, T. and Hoefnagels JPM. (2022). Plasticity, localization, and damage in ferritic-pearlitic steel studied by nanoscale digital image correlation. Scripta Materialia, 208, 114327. DOI: https://doi.org/10.1016/j.scriptamat.2021.114327.

[15] Zhou, L., Fang, F., Wang, L., Chen, H., Xie, Z. and Jiang J. (2018) Torsion delamination and recrystallized cementite of heavy drawing pearlitic wires after low temperature annealing. Mater. Sci. Eng. A, 713, pp. 52–60. DOI: https://doi.org/10.1016/j.msea.2017.12.055.

[16] Tsuchida, N., Inoue, T., Nakano, H., Okamoto, T. (2015). Enhanced true stress–true strain relationships due to grain refinement of a low-carbon ferrite–pearlite steel. Materials Letters 160, pp. 117–119. DOI: https://doi.org/10.1016/j.matlet.2015.07.093.

[17] Mediratta, S.R., Ramaswamy, V., Rama Rao P. (1986). Two stage cyclic work hardening and two slope coffin-manson relationship in dual phase steels. Scripta Metallurgica 1986;20(4), pp. 555–558. DOI: https://doi.org/10.1016/0036-9748(86)90253-X.

[18] Majumdar, S., Gandhi A.D, Bisht M.S. (2019). Low cycle fatigue behaviour of a ferritic steel strengthened with nano-meter sized precipitates. Mater. Sci. Eng. A, 756, pp. 198–212. DOI: https://doi.org/10.1016/j.msea.2019.04.043.

[19] Majumdar, S., Bhattacharjee, D., Ray, K.K. and Ray, R.K. (2013). Bilinear Coffin–Manson Relationship in Thin Sheets of Interstitial-Free Steel. Metall Mater Trans A 2013;44(4), pp. 1714–1721. DOI: https://doi.org/10.1007/s11661-012-1514-9.7

[20] Korda, A.A., Mutoh, Y., Miyashita, Y. and Sadasue T. (2006). Effects of pearlite morphology and specimen thickness on fatigue crack growth resistance in ferritic–pearlitic steels. Materials Science and Engineering: A 428(1-2), pp. 262–269.
[21] Das Bakshi, S., Javed, N., Sasidhar, K.N., Dhande, T., Sharma, V. and Mukherjee, M.(2018). Effect of microstructure and crystallographic texture on mechanical anisotropy of Ti-Nb microalloyed hot rolled 800 MPa HSLA steel. Materials Characterization. 136(12), pp. 346–357. DOI: https://doi.org/10.1016/j.matchar.2017.12.039.
[22] Chen,Y., Wu, Z., Wu, G., Wang, N., Zhao, Q. and Luo, J. (2020) Investigation on micromechanism of ferrite hardening after pre-straining with different strain rates of dual-phase steel. Mater. Sci. Eng. A. 802(2), 140657. DOI: https://doi.org/10.1016/j.msea.2020.140657.
[23] Lu, D., Lin, B., Liu, T., Deng, S., Guo, Y., Li J. (2023). Effect of grain structure on fatigue crack propagation behavior of Al-Cu-Li alloys. Journal of Materials Science & Technology. 148, pp.75–89. DOI: https://doi.org/10.1016/j.jmst.2022.10.085.
[24] Zhao, Y., Zhang, B., Si, Y., Ding, S., Sun, Q., Yang, K. (2025). Microstructural characterization and low-cycle fatigue behavior of ODS steel prepared by precursor-assisted cast technology. Nuclear Materials and Energy. 43(4), 101933. DOI: https://doi.org/10.1016/j.nme.2025.101933.
[25] Wang, Z., Yuan, Q., Zhang, Z., Zhang. Q. and Xu, G. (2022). Influence of Cementite Precipitation on Work Hardening Behavior in Ultrafine Grain Steels Rolled at Room and Cryogenic Temperatures. Metals. 12(11), 1845. DOI: https://doi.org/10.3390/met12111845.
[26] Yonezawa, T., Mori, T. and Tsutsumi, S. (2024). Effects of Cyclic Softening on Fatigue Crack Propagation Properties of Steel. ISIJ Int. 64(3), pp. 605–612. DOI: https://doi.org/10.2355/isijinternational.ISIJINT-2023-428.
[27] Wanni, J., Colak, A. and Achuthan, A. (2023). Subgrain microstructural features in directed energy deposited stainless steel 316L: The influence of morphology on mechanical properties. Mater. Sci.Eng. A. 880(9), 145215. DOI: https://doi.org/10.1016/j.msea.2023.145215.
[28] Chauhan, A., Bergner, F., Etienne, A., Aktaa, J., de Carlan, Y. and Heintze, C. (2017). Microstructure characterization and strengthening mechanisms of oxide dispersion strengthened (ODS) Fe-9%Cr and Fe-14%Cr extruded bars. Journal of Nuclear Materials. 495, pp. 6–19. DOI: https://doi.org/10.1016/j.jnucmat.2017.07.060.
[29] Cruzado, A., Lucarini, S., LLorca, J., and Segurado, J. (2018). Microstructure-based fatigue life model of metallic alloys with bilinear Coffin-Manson behavior. International Journal of Fatigue. 107(6), pp. 40–48. DOI: https://doi.org/10.1016/j.ijfatigue.2017.10.014.